

Incremental Nonlinear Control Allocation for an Aircraft with Distributed Electric Propulsion

de Heer, P.; de Visser, C.C.; Hoogendoorn, M.L.; Jentink, Henk W

DOI

[10.2514/6.2023-1248](https://doi.org/10.2514/6.2023-1248)

Publication date

2023

Document Version

Final published version

Published in

AIAA SciTech Forum 2023

Citation (APA)

de Heer, P., de Visser, C. C., Hoogendoorn, M. L., & Jentink, H. W. (2023). Incremental Nonlinear Control Allocation for an Aircraft with Distributed Electric Propulsion. In *AIAA SciTech Forum 2023* Article AIAA 2023-1248 <https://doi.org/10.2514/6.2023-1248>

Important note

To cite this publication, please use the final published version (if applicable). Please check the document version above.

Copyright

Other than for strictly personal use, it is not permitted to download, forward or distribute the text or part of it, without the consent of the author(s) and/or copyright holder(s), unless the work is under an open content license such as Creative Commons.

Takedown policy

Please contact us and provide details if you believe this document breaches copyrights. We will remove access to the work immediately and investigate your claim.

Incremental Nonlinear Control Allocation for an Aircraft with Distributed Electric Propulsion

P. de Heer* and C.C. de Visser†
Delft University of Technology, 2629HS Delft, The Netherlands

M.L. Hoogendoorn‡ and H.W. Jentink§
NLR - Royal Netherlands Aerospace Centre, 1059 CM Amsterdam, the Netherlands

In this paper, a new nonlinear control allocation method is presented for a distributed electric propulsion (DEP) aircraft. As the electric propellers can be used actively for control, in addition to the control surfaces, the DEP aircraft is over-actuated. This freedom in control effectors can be exploited with an appropriate control allocation method. All control effectors are, therefore, captured in the incremental nonlinear control allocation (INCA) method, which allows taking into account effector nonlinearities and interactions introduced by the propellers. The INCA method is based on a real-time updated Jacobian model of the control effectiveness, thereby solving an efficient linear control allocation problem. This paper reformulates the original INCA method to optimize the control allocation for minimal propeller power, resulting in more efficient flight. A model predictive control (MPC) controller is added as an actuator dynamics compensation method. This ensures that the commanded control inputs from the INCA controller are achieved. The new controller is compared to a standard incremental nonlinear dynamic inversion (INDI) controller with a translational and rotational loop. It is shown in simulation that by combining INCA with MPC, the tracking performance is improved and efficiency increased by 6.1%.

I. Nomenclature

A_x, A_y, A_z	=	external accelerations in body frame
AR	=	aspect ratio
b	=	wing span
C	=	dimensionless coefficient
\bar{c}	=	mean aerodynamic chord
D	=	drag
e	=	span-wise efficiency parameter
\mathcal{F}	=	force vector
F_a, F_b, F_E, F_V	=	aerodynamic, body, vehicle-carried normal Earth and velocity frame
g	=	gravitational acceleration
h	=	altitude
\mathbf{I}	=	inertia matrix
J	=	advance ratio
\mathbf{K}	=	proportional gain matrix
L	=	lift
l, m, n	=	aerodynamic moments in the body frame
m	=	mass
\mathcal{M}	=	moment vector
n_p	=	propeller rotational velocity

*MSc student, DCSC, Faculty of Mechanical, Maritime and Materials Engineering, 2628 CN Delft, The Netherlands, pepijndeheer@gmail.com.

†Assistant Professor, Control and Simulation Division, Faculty of Aerospace Engineering, Kluyverweg 1, 2629HS Delft, The Netherlands, c.c.devisser@tudelft.nl, AIAA Member.

‡Medior R&D Engineer, Flight Test and Certification, Anthony Fokkerweg 2, 1059 CM Amsterdam, The Netherlands, Marijn.Hoogendoorn@nlr.nl.

§Senior Scientist, Flight Test and Certification, Anthony Fokkerweg 2, 1059 CM Amsterdam, The Netherlands, Henk.Jentink@nlr.nl.

P_p	=	propeller power
p, q, r	=	roll, pitch and yaw rate
q	=	dynamic pressure
S	=	wing surface
t	=	time
T_p	=	propeller thrust
\mathbf{u}	=	control input vector
u, v, w	=	airspeed components in body frame
V_∞	=	true airspeed
\mathbf{x}	=	state vector
X, Y, Z	=	aerodynamic and propulsive forces
\mathbf{y}	=	output vector
α	=	angle of attack
β	=	angle of sideslip
γ	=	flight path angle
δ	=	control surface deflections
λ	=	perturbation term
\mathbf{v}	=	virtual control input
ζ	=	damping coefficient
ρ	=	air density
$\boldsymbol{\tau}$	=	control force and moment vector
Φ	=	control forces and moments mapping
ϕ, θ, ψ	=	roll, pitch and yaw angle
χ	=	kinematic azimuth angle
Ω	=	propeller power mapping
$\boldsymbol{\omega}$	=	angular rates in body frame
ω_n	=	natural frequency
∇	=	Jacobian
Subscripts		
a	=	actual
c	=	commanded
des	=	desired
h	=	hedge
ref	=	reference
rm	=	reference model

II. Introduction

IF no significant measures are taken, aircraft CO₂ emissions will triple by 2050. This is due to an increase in aircraft traffic, which historically doubles every fifteen years [1]. As a result, more demanding requirements on fuel consumption, noise and chemical emissions are set, which calls for radically new aircraft concepts. The uncertainty for these new designs increases, because less historical data is available. A scaled flight demonstrator (SFD), therefore, forms a valuable addition to the design process, reducing the risks in terms of time and costs compared to full-scale testing. At Royal Netherlands Aerospace Centre (NLR), in collaboration with Clean Sky 2 [2] partners ONERA, CIRA, Airbus and Orange Aerospace BV, such an SFD is developed. Here a scaled 1:8.5 model of the Airbus A320 [3] is tested, which forms the baseline on which new aircraft design concepts will be developed.

A promising new propulsion technique that is being researched, is distributed electric propulsion (DEP). For this concept, the two jet engines of the Airbus A320 are replaced with six electric propellers, three on each wing. Similar projects developing this technology include the NASA Sceptor project for the NASA X-57 aircraft [4] and the NASA STTR project with a Cirrus SR22T scale model [5]. Besides key advantages in terms of aircraft design, it is interesting to note that electric propellers have relatively low control input lags, which means that they can be used actively for control [5]. Integration of the propellers results in coupling effects between the aerodynamics and propulsion, also known as propulsion airframe interaction (PAI) effects. Together with differential thrust, this gives extra control freedom which potentially improves flight performance, efficiency and robustness against actuator failures of aircraft [6]. The

control aspect of DEP aircraft received limited attention in previous research, only modeling differential thrust [7, 8] or designing a simple proportional–integral–derivative (PID) controller, without actively using the PAI effects [9]. Including the PAI effects poses a significant challenge, since this introduces nonlinear behavior and cross-couplings, which are difficult to model accurately [10]. Furthermore, the introduction of extra control effectors introduces the need for a control allocation method, as the aircraft becomes over-actuated [11]. This gave rise to the research into a control method that can actively use all control effectors of the DEP aircraft while being robust against modeling errors. As the aircraft and PAI effects dynamics are nonlinear, a nonlinear controller is required.

A common nonlinear control method for aircraft is nonlinear dynamic inversion (NDI) [12, 13]. A downside of this method is that it relies completely on the aircraft model. Achieving robustness against modeling errors is, therefore, challenging at best, and comes at the cost of reduced tracking performance. For this reason, the incremental counterpart incremental nonlinear dynamic inversion (INDI) [14] forms a suitable alternative. For this method, the incremental control input is calculated based on sensor measurements. If sampled at a sufficiently high frequency, part of the aircraft’s model can be discarded, making the control law less model-dependent. As the sensor measurements also contain external disturbances, the controller compensates for their influences, making it more robust. However, for this type of controller to work, time derivatives of the controlled variables are required, given by nonlinear state observers or a new class of inertial sensors as angular accelerometers [15, 16].

Another important aspect is that a suitable control allocation method is required for the DEP aircraft, since it is over-actuated. A simple method for this is ganging, but this leads to sub-optimal allocation [17]. Other techniques can be classified into linear and nonlinear allocation. The latter can take into account nonlinear relations, and examples of this include nonlinear direct allocation [18], modeling with piecewise linear functions [19] and nonlinear optimization using nonlinear programming [20]. Although all these methods show a significant improvement in terms of performance, they are computationally demanding, so they cannot run in real time [21]. Linear allocation methods are, therefore, a better alternative in terms of implementation. Common linear methods found in literature include the weighted generalized inverse [17], redistributed pseudo-inverse [22], daisy-chaining [23] and direct allocation [24]. Also, optimization-based methods such as linear (LP) and quadratic programming (QP) can be used to solve the allocation problem [25]. A major shortcoming of these linear techniques is that they assume a linear relationship between the control forces and moments and the control effectors. Furthermore, interactions between the effectors cannot be taken into account. As the PAI effect introduces both nonlinearities and interactions, linear control allocation is not able to take full advantage of the DEP system. A viable alternative is proposed in [21], where the method of INDI is combined with linear optimization allocation. This allows taking into account nonlinearities and effector interactions while solving an efficient linear allocation problem online. Using the mixed optimization problem with QP [25], the allocation is optimized for tracking and another secondary objective.

The main contribution of this paper is the design of a new nonlinear control allocation method, which takes into account all control effectors of the DEP aircraft, while optimizing for minimal propeller power. It extends on the INCA method by redefining the secondary objective to optimize for minimal propeller power. This enables optimal exploitation of the differential thrust and PAI effects. Furthermore, the INCA control scheme is extended with a translational control loop, allocating the control inputs for altitude and velocity control next to attitude control. Finally, the INCA controller is augmented with a model predictive control (MPC) controller to compensate for the actuator dynamics, based on the work in [26]. This method is redesigned, so that it can compensate incrementally, ensuring that the commanded incremental control inputs are achieved. To assess the performance of the new controller, it will be compared against the conventional NDI/INDI controller in [27], which presents control loops for translational and rotational control.

The outline of this paper is as follows. First, the DEP aircraft model including the differential thrust and PAI effects will be described in Sec. III. In Sec. IV, the NDI and INDI control laws will be derived, which are used in Sec. V to define the control laws for the DEP aircraft. Sec. VI explores the potential performance increase because of over-actuation, designing a suitable control allocation method that optimizes for propeller power. Finally, in Sec. VII the results found in simulation are presented and compared against the conventional NDI/INDI controller, after which the paper is concluded in Sec. VIII.

III. DEP Aircraft Model

The aircraft model used in this paper is based on the model developed for the SFD [3]. Added to this model are the differential thrust and PAI effects, which are introduced by the six electric propellers. The DEP aircraft uses the traditional control surfaces ailerons, elevator and rudder for roll, pitch and yaw control respectively. Next to this, the six propellers can be used for both roll and yaw control. If the propellers operate at different thrust levels, the differential

thrust effect creates a yawing moment. Furthermore, an increase in propeller thrust results in a local increase in lift, thereby providing roll control using the PAI effects. The effects of the control inputs are summarized in Fig. 1, given in the body reference frame (F_b).

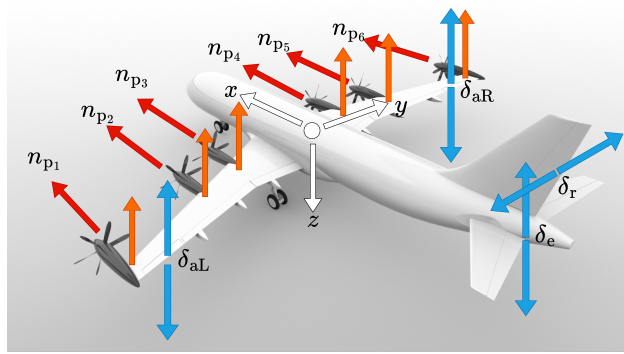


Fig. 1 Overview of the control input effects on the DEP aircraft, where the blue arrows represent the control surface deflections, the red the differential thrust effects and the orange the PAI effects in the F_b frame.

As all six propeller are controlled separately, this gives the following control input vector

$$\mathbf{u} = \left[\delta_{aL} \quad \delta_{aR} \quad \delta_e \quad \delta_r \quad n_{p1} \quad n_{p2} \quad n_{p3} \quad n_{p4} \quad n_{p5} \quad n_{p6} \right]^T, \quad (1)$$

where n_p is the rotational velocity of the propellers and δ the control surface deflection. The left δ_{aL} and right δ_{aR} aileron are controlled separately. The control inputs \mathbf{u} are subject to position and rate constraints, which are defined as

$$\begin{aligned} \mathbf{u}_{\min} &\leq \mathbf{u} \leq \mathbf{u}_{\max}, \\ |\dot{\mathbf{u}}| &\leq \dot{\mathbf{u}}_{\max}. \end{aligned} \quad (2)$$

All control inputs are also subject to actuator dynamics, which are modeled using a second-order transfer function $A(s)$ defined as

$$A(s) = \frac{\omega_n^2}{s^2 + \zeta\omega_n s + \omega_n^2}, \quad (3)$$

where ω_n is the natural frequency and ζ the damping coefficient of the actuator. The constraints and actuator dynamics values for each actuator are given in Table 1 and Table 2.

Table 1 Control input constraints.

Limit	δ_{aL}	δ_{aR}	δ_e	δ_r	n_p
u_{\min}	-25°	-25°	-15°	-30°	0 rev/s
u_{\max}	25°	25°	30°	30°	100 rev/s
\dot{u}_{\max}	$243^\circ/s$	$243^\circ/s$	$207^\circ/s$	$207^\circ/s$	100 rev/s^2

Table 2 Actuator dynamics.

Second-order dynamics	δ_{aL}	δ_{aR}	δ_e	δ_r	n_p
ω_n	6.460	6.460	5.680	5.680	6.000
ζ	0.821	0.821	0.859	0.859	0.850

To model the PAI effects, first, the propellers need to be described using the thrust C_T and power C_P coefficients [28]. These are a function of the advance ratio J and were determined using experimental data shown in Fig. 19 and Fig. 20. Based on these coefficients, the propeller thrust T_p and propeller power P_p can be determined as a function of the true airspeed V_∞ and propeller rotational velocity n_p .

As discussed in [29], for propellers placed in front of the wing two effects can be identified, the propeller affecting the wing and other aerodynamic surfaces and vice versa. As the first effect is most significant for propellers placed in front of the wing, changing the control force \mathcal{F}_c and moment vector \mathcal{M}_c , this is the only effect that will be considered in the remainder of this paper. The propellers affect the slipstream over the wing, consisting of an axial and swirl component. To analyze the effect of this change in the slipstream, the method of [30] is used. It discards the swirl component effects of the slipstream and assumes that the increase in axial velocity behind the propeller is uniform. The changes in lift ΔC_L and drag ΔC_D coefficient are then calculated based on an increase in dynamic pressure q , using actuator disk theory. Note that as the slipstream is finite, a correction factor is applied using the surrogate model of [31]. The same method is used to calculate the dynamic pressure increase behind the outer propeller's slipstream, increasing the effectiveness of the ailerons.

Another important element of the PAI effects is the interaction between the wingtip propellers and vortices. The propellers cancel out these vortices, reducing the induced drag defined as

$$C_{Di} = \frac{C_L^2}{\pi A R e}. \quad (4)$$

As no aerodynamic data is available for the DEP aircraft, the wind tunnel data in [32] is used as reference. This research finds a relation between the thrust coefficient C_T and the spanwise efficiency factor e . The results are scaled to the C_T operating values of the DEP aircraft, which is summarized in Table 3. An increase in C_T thus gives an increase e , reducing the induced drag, where the maximum increase in e is assumed to be $e_{\max} = 1.12$.

Table 3 Relationship between C_T and e from wind tunnel test data scaled to the DEP aircraft.

	Sinnige et al. [32]		DEP	
	C_T	e	C_T	e
min	0	0.8	0	0.8
optimum	0.123	1.12 (+40%)	0.267	1.12 (+40%)
max	0.168	0.68 (-15%)	0.365	1.12 (+40%)

IV. Nonlinear Flight Control Design

The general nonlinear aircraft dynamics expressed in the input-affine form [12] are given by

$$\begin{aligned} \dot{\mathbf{x}} &= \mathbf{f}(\mathbf{x}) + \mathbf{g}(\mathbf{x})\mathbf{u}, \\ \mathbf{y} &= \mathbf{x}, \end{aligned} \quad (5)$$

where $\mathbf{x} \in \mathbb{R}^n$ is the state vector, $\mathbf{u} \in \mathbb{R}^p$ the control input vector and $\mathbf{y} \in \mathbb{R}^m$ the output vector. Note that it is thus assumed that all states \mathbf{x} are directly available. $\mathbf{f} \in \mathbb{R}^n$ and $\mathbf{g} \in \mathbb{R}^{n \times p}$ are nonlinear functions depending only on the state \mathbf{x} . For the remainder of this section it is assumed that the number of inputs equals the number of outputs, so that $\mathbf{g} \in \mathbb{R}^{n \times m}$, which is a square matrix for full-state measurement. A control allocation method to fully take into account the over-actuated DEP aircraft will be developed in the next section. To control the nonlinear dynamics of Eq. (5) types of controllers are used, namely NDI and INDI.

A. Nonlinear dynamic inversion

The NDI controller is defined by introducing the virtual control input \mathbf{v} and setting this equal to the derivative of the output, so that $\mathbf{v} = \dot{\mathbf{y}} = \dot{\mathbf{x}}$. The control input is then defined by inverting the dynamics of Eq. (5) so that

$$\mathbf{u} = \mathbf{g}^{-1}(\mathbf{x}) (\mathbf{v}(\mathbf{x}) - \mathbf{f}(\mathbf{x})), \quad (6)$$

which gives the closed loop relation

$$\dot{\mathbf{y}} = \mathbf{v}(\mathbf{x}). \quad (7)$$

The virtual control input \mathbf{v} is determined using a linear controller with proportional gain \mathbf{K} , steering the states \mathbf{x} to the reference states \mathbf{x}_{ref} , which is defined as

$$\mathbf{v}(\mathbf{x}) = \mathbf{K} (\mathbf{x}_{\text{ref}} - \mathbf{x}). \quad (8)$$

Note that for Eq. (7) to hold, the exact model should be known to completely linearize the dynamics. In reality, modeling uncertainties, computational errors and external disturbances introduce inversion errors. These can be captured in the perturbation term λ , so that the closed loop system becomes

$$\dot{\mathbf{y}} = \mathbf{v}(\mathbf{x}) + \lambda(\mathbf{x}). \quad (9)$$

Robustness against this perturbation term is not guaranteed which can come at the cost of reduced tracking performance or instability.

B. Incremental nonlinear dynamic inversion

INDI can be used as an alternative to NDI, as this method is more robust against the influences of the perturbation term λ . This controller will be derived without the time-scale separation principle, following the method of [33]. In this more general form, as compared to the traditional derivation given in [14], there is more freedom in the design of the control loops. This freedom will be used for simultaneous translational and rotational control, which will be discussed in Sec. VI.B.

Consider the input affine aircraft dynamics of Eq. (5), taking the first-order Taylor expansion gives

$$\begin{aligned} \dot{\mathbf{y}} &= \dot{\mathbf{y}}_0 + \left. \frac{\partial [\mathbf{f}(\mathbf{x}) + \mathbf{g}(\mathbf{x})\mathbf{u}]}{\partial \mathbf{x}} \right|_0 \Delta \mathbf{x} + \left. \frac{\partial [\mathbf{f}(\mathbf{x}) + \mathbf{g}(\mathbf{x})\mathbf{u}]}{\partial \mathbf{u}} \right|_0 \Delta \mathbf{u} + O(\Delta \mathbf{x}^2), \\ \dot{\mathbf{y}} &= \dot{\mathbf{y}}_0 + \left. \frac{\partial [\mathbf{f}(\mathbf{x}) + \mathbf{g}(\mathbf{x})\mathbf{u}]}{\partial \mathbf{x}} \right|_0 \Delta \mathbf{x} + \mathbf{g}(\mathbf{x}_0)\Delta \mathbf{u} + O(\Delta \mathbf{x}^2). \end{aligned} \quad (10)$$

Again, the perturbation term λ is introduced, which now also captures errors caused by the Taylor expansion, so that

$$\dot{\mathbf{y}} = \dot{\mathbf{y}}_0 + \mathbf{g}(\mathbf{x}_0)\Delta \mathbf{u} + \lambda(\mathbf{x}, \Delta t), \quad (11)$$

where

$$\lambda(\mathbf{x}, \Delta t) = \left. \frac{\partial [\mathbf{f}(\mathbf{x}) + \mathbf{g}(\mathbf{x})\mathbf{u}]}{\partial \mathbf{x}} \right|_0 \Delta \mathbf{x} + O(\Delta \mathbf{x}^2). \quad (12)$$

Setting $\mathbf{v} = \dot{\mathbf{x}}$ defined by Eq. (8), the incremental and total control input is defined by inverting Eq. (11) so that,

$$\begin{aligned} \Delta \mathbf{u} &= \mathbf{g}^{-1}(\mathbf{x}_0) (\mathbf{v}(\mathbf{x}) - \dot{\mathbf{y}}_0), \\ \mathbf{u} &= \mathbf{u}_0 + \Delta \mathbf{u}_0, \end{aligned} \quad (13)$$

which gives the closed loop relation

$$\dot{\mathbf{y}} = \mathbf{v}(\mathbf{x}) + \lambda(\mathbf{x}, \Delta t). \quad (14)$$

Comparing Eq. (9) with Eq. (14), one can see that for the latter the perturbation term λ also depends on Δt . As is shown in [33] for INDI, there exists a bound on the perturbation term λ and this bound is decreased with decreasing sampling time Δt . This shows for relations involving perturbation influences, the performance of INDI is superior to NDI when the sampling frequency is sufficiently high. This is under the assumption that $\dot{\mathbf{y}}_0$ is either directly measured or obtained through (predictive) differentiation.

C. Pseudo-control hedging

To prevent windup problems for unachievable control commands, pseudo-control hedging (PCH) is implemented [34]. The idea of PCH is to hedge the control signal with the difference between the commanded and achieved control input. This difference develops when the commanded control forces and moments for tracking of the reference variables cannot be achieved by the actuators. It is defined as the pseudo-control hedge and is given by

$$\mathbf{v}_h(\mathbf{x}) = \mathbf{v}_c(\mathbf{x}) - \hat{\mathbf{y}}(\mathbf{x}), \quad (15)$$

where $\mathbf{v}_c(\mathbf{x})$ is the commanded and $\hat{\mathbf{v}}(\mathbf{x})$ the estimated achieved virtual control input, which is based on the measured actuator states. To hedge the control signal, a first-order reference model is defined as

$$\mathbf{v}_{rm} = \mathbf{K}_{rm}(\mathbf{x}_c - \mathbf{x}_{rm}), \quad (16)$$

where \mathbf{K}_{rm} is a diagonal matrix containing the reference model gains, \mathbf{x}_c is the commanded and \mathbf{x}_{rm} the reference model state vector. The reference signal sent to the control system is \mathbf{x}_{rm} , and this state vector is given by

$$\dot{\mathbf{x}}_{rm} = \frac{1}{s}(\mathbf{v}_{rm} - \mathbf{v}_h). \quad (17)$$

When there is no saturation $\mathbf{v}_h = 0$, as there is no difference between the commanded and actual virtual control input. For this situation, the reference model acts as low-pass filter with bandwidth K_{rmi} for the i -th state of \mathbf{x}_c . When there is saturation, \mathbf{v}_h will give the difference between the commanded and achieved virtual control input, as defined in Eq. (15). The PCH for incremental control [21] is defined by substituting Eq. (11), disregarding the perturbation term λ , in Eq. (15) which gives

$$\begin{aligned} \mathbf{v}_h &= [\dot{\mathbf{y}}_0 + \mathbf{g}(\mathbf{x}_0)(\mathbf{u}_c - \mathbf{u}_0)] - [\dot{\mathbf{y}}_0 + \mathbf{g}(\mathbf{x}_0)(\mathbf{u} - \mathbf{u}_0)], \\ &= \mathbf{g}(\mathbf{x}_0)(\mathbf{u}_c - \mathbf{u}). \end{aligned} \quad (18)$$

To improve tracking performance, the derivatives of the reference commands, as defined in Eq. (16), are used as feedforward terms [35]. In the subsequent sections, the different control loops for translational and rotational control are derived.

V. Traditional Aircraft Control Loops

In this section, the control loops for traditional aircraft control are derived, using the control surfaces δ for rotational control and the total thrust T_{tot} to control the velocity. Note that the thrust of all propellers is thus the same in this definition, so that $T_{tot} = T_{p1} + T_{p2} + \dots + T_{p6}$. This means the differential thrust and PAI effects are not included yet, as this requires control allocation and will be discussed in the subsequent section.

The reference values for control of the DEP aircraft are defined as

$$\mathbf{y}_{ref} = \begin{bmatrix} V_{ref} & h_{ref} & \phi_{ref} & \beta_{ref} \end{bmatrix}^T, \quad (19)$$

so that the reference altitude h , velocity V , roll angle ϕ and sideslip angle β are tracked. By default, $\beta_{ref} = 0$ so that the angle of sideslip is minimized, which gives coordinated turns and leads to most efficient flight.

Following [27], four different loops are used to control the aircraft, which are divided based on the the time-scale separation principle. This states that slower outer loops and faster inner loops can be controlled individually, as long as each subsequent loop is faster than the preceding loop. The following state variables are defined

$$\begin{aligned} \mathbf{x}_1 &= \begin{bmatrix} V & \chi & \gamma \end{bmatrix}^T, \bar{\mathbf{x}}_1 = \begin{bmatrix} V & \gamma \end{bmatrix}^T, \\ \mathbf{x}_2 &= \begin{bmatrix} \phi & \alpha & \beta \end{bmatrix}^T, \\ \mathbf{x}_3 &= \begin{bmatrix} p & q & r \end{bmatrix}^T, \end{aligned} \quad (20)$$

where V is the true airspeed, χ the kinematic azimuth angle, γ the flight path angle, ϕ the roll angle, α the angle of attack, β the angle of sideslip and p , q and r the roll, pitch and yaw rate respectively. The control inputs for the separate control loops are defined as

$$\begin{aligned} \mathbf{u}_1 &= \begin{bmatrix} \alpha_{des} & T_{tot} \end{bmatrix}^T, \\ \mathbf{u}_3 &= \begin{bmatrix} \delta_a & \delta_e & \delta_r \end{bmatrix}^T, \end{aligned} \quad (21)$$

where α_{des} represents the desired angle of attack, which cannot be reached instantaneously because of the dynamics of the aircraft. The control loop structure with the four different controllers is shown in Fig. 2. For the loops involving only kinematic relations, the NDI method is used as these do not contain modeling errors or external disturbances. Dynamic relations are controlled using the INDI method to make the control law more robust. Also, as the dynamic relations contain control commands \mathbf{u}_1 and \mathbf{u}_3 , PCH will be applied for these loops. In the subsequent sections, the subscript *ref* is used for reference commands which the aircraft is to follow and the subscript *des* for desired commands generated by the controller.

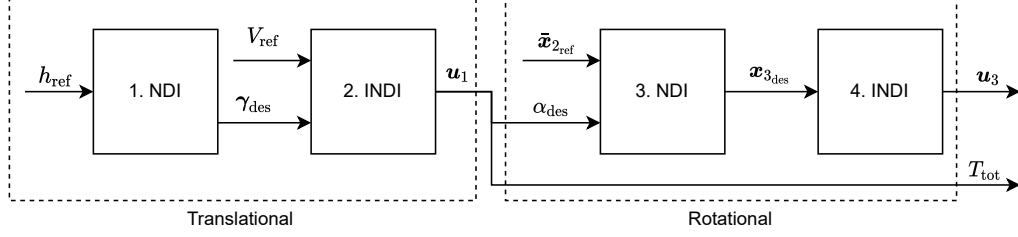


Fig. 2 Control loop structure for translational (block 1 and 2) and rotational (block 3 and 4) control.

A. Translational Control Loop

1. Altitude Control Loop

In controller 1 of Fig. 2, the desired flight path angle γ_{des} is determined, based on h_{ref} , using the kinematic relation

$$\dot{h} = V \sin \gamma. \quad (22)$$

Setting the virtual control input $v_h = \dot{h}_{\text{des}}$, based on the tracking error of h_{ref} , gives the desired flight path angle as

$$\gamma_{\text{des}} = \arcsin \left(\frac{v_h}{V_{\text{ref}}} \right). \quad (23)$$

2. Flight Path Angle and Velocity Control Loop

Controller 2 in Fig. 2 controls $\bar{\mathbf{x}}_1$, where the values V_{ref} and γ_{des} are used as reference values. The dynamics for \mathbf{x}_1 are defined as

$$\dot{\mathbf{x}}_1 = \begin{bmatrix} \frac{1}{m} & 0 & 0 \\ 0 & \frac{1}{mV \cos \gamma} & 0 \\ 0 & 0 & -\frac{1}{mv} \end{bmatrix} \left(\mathbf{T}_{\text{Va}} \begin{bmatrix} X_a \\ Y_a \\ Z_a \end{bmatrix} + \mathbf{T}_{\text{VE}} \begin{bmatrix} 0 \\ 0 \\ mg \end{bmatrix} \right), \quad (24)$$

where the vector $[X_a, Y_a, Z_a]^T$ contains the aerodynamic and propulsive forces in the aerodynamic reference frame (F_a) [36]. The matrices \mathbf{T}_{Va} and \mathbf{T}_{VE} are transformation matrices, where F_V is the velocity and F_E the vehicle-carried normal Earth reference frame [27]. As χ will not be controlled, instead the roll angle ϕ_{ref} is specified in \mathbf{y}_{ref} , only the first and third row of Eq. (24) are considered. Eq. (24) can be rewritten in the affine-in-control form for \mathbf{u}_1 [27], so that

$$\dot{\bar{\mathbf{x}}}_1 = \bar{\mathbf{f}}_1(\mathbf{x}) + \bar{\mathbf{g}}_1(\mathbf{x})\mathbf{u}_1. \quad (25)$$

Setting the virtual control input $v_{\bar{\mathbf{x}}_1} = \dot{\bar{\mathbf{x}}}_{1,\text{des}}$ for tracking of V_{ref} and γ_{des} , the INDI controller is defined as

$$\begin{aligned} \Delta \mathbf{u}_1 &= \bar{\mathbf{g}}_1^{-1}(\mathbf{x}_0) (v_{\bar{\mathbf{x}}_1} - \dot{\bar{\mathbf{x}}}_{1,0}), \\ \mathbf{u}_1 &= \mathbf{u}_{1,0} + \Delta \mathbf{u}_1. \end{aligned} \quad (26)$$

PCH is implemented for this control loop, with the pseudo-control hedge defined as

$$v_{h_{\mathbf{x}_1}} = \mathbf{g}_1(\mathbf{x}_0) (\mathbf{u}_{1,c} - \mathbf{u}_1). \quad (27)$$

B. Rotational Control Loop

1. Aerodynamic Attitude Control Loop

Controller 3 in Fig. 2, controls \mathbf{x}_2 with ϕ_{ref} , α_{des} and β_{ref} as reference. The kinematic relation between \mathbf{x}_2 and \mathbf{x}_3 , given in [37, 38], is defined as

$$\dot{\mathbf{x}}_2 = \underbrace{\begin{bmatrix} 0 \\ \left(\frac{1}{u^2+w^2} \right) (u (A_z + g \cos \theta \cos \phi) - w (A_x - g \sin \theta)) \\ \left(\frac{1}{\sqrt{u^2+w^2}} \right) (F_x + F_y + F_z) \end{bmatrix}}_{\mathbf{b}_{\mathbf{x}_2}(\mathbf{x})} + \underbrace{\begin{bmatrix} 1 & \sin \phi \tan \theta & \cos \phi \tan \theta \\ \frac{-uv}{u^2+w^2} & 1 & \frac{-vw}{u^2+w^2} \\ \frac{w}{\sqrt{u^2+w^2}} & 0 & \frac{-u}{\sqrt{u^2+w^2}} \end{bmatrix}}_{\mathbf{a}_{\mathbf{x}_2}(\mathbf{x})} \mathbf{x}_3, \quad (28)$$

where u, v, w are the airspeed components in the F_b frame, θ the pitch angle and A_x, A_y, A_z the external accelerations in the F_b frame and

$$\begin{aligned} F_x &= -\frac{uv}{V^2}(A_x - g \sin \theta), \\ F_y &= \left(1 - \frac{v^2}{V^2}\right)(A_y + g \sin \phi \cos \theta), \\ F_z &= -\frac{vw}{V^2}(A_z + g \cos \phi \cos \theta). \end{aligned} \quad (29)$$

Applying NDI by setting $\mathbf{v}_{x_2} = \dot{\mathbf{x}}_{2_{\text{des}}}$ for tracking of $\phi_{\text{ref}}, \alpha_{\text{des}}$ and β_{ref} gives

$$\mathbf{x}_{3_{\text{des}}} = \mathbf{a}_{x_2}^{-1}(\mathbf{x})(\mathbf{v}_{x_2} - \mathbf{b}_{x_2}(\mathbf{x})). \quad (30)$$

2. Body Angular Rate Control Loop

Finally, controller 4 in Fig. 2 controls \mathbf{x}_3 using the desired body angular rates as reference. The dynamics of the angular rates \mathbf{x}_3 are defined as

$$\dot{\mathbf{x}}_3 = \mathbf{I}^{-1}(\mathbf{M} - \mathbf{x}_3 \times \mathbf{I} \mathbf{x}_3), \quad (31)$$

where \mathbf{M} contains all the moments applied to the aircraft in the F_b frame and \mathbf{I} is the moment of inertia matrix [36]. The moments can be separated into the ones applied by the airframe \mathbf{M}_a , and by the control inputs \mathbf{M}_c . Also, for more compact notation, define the state dependent part as

$$\mathbf{f}_3(\mathbf{x}) = \mathbf{I}^{-1}(\mathbf{M}_a - \mathbf{x}_3 \times \mathbf{I} \mathbf{x}_3), \quad (32)$$

so that

$$\dot{\mathbf{x}}_3 = \mathbf{f}_3(\mathbf{x}) + \mathbf{I}^{-1} \mathbf{M}_c. \quad (33)$$

In the affine-in-control form this becomes

$$\dot{\mathbf{x}}_3 = \mathbf{f}_3(\mathbf{x}) + \mathbf{g}_3(\mathbf{x}) \mathbf{u}_3. \quad (34)$$

By setting $\mathbf{v}_{x_3} = \dot{\mathbf{x}}_{3_{\text{des}}}$ for tracking of $p_{\text{des}}, q_{\text{des}}$ and r_{des} , the INDI controller is defined as

$$\begin{aligned} \Delta \mathbf{u}_3 &= \mathbf{g}_3^{-1}(\mathbf{x}_0)(\mathbf{v}_{x_3} - \dot{\mathbf{x}}_{3,0}) \\ \mathbf{u}_3 &= \mathbf{u}_{3,0} + \Delta \mathbf{u}_3. \end{aligned} \quad (35)$$

PCH is implemented for this control loop with the pseudo-control hedge defined as

$$\mathbf{v}_{h_{x_3}} = \mathbf{g}_3(\mathbf{x}_0)(\mathbf{u}_{3_c} - \mathbf{u}_3). \quad (36)$$

VI. Control Allocation Design

Generally, the control forces and moments are a nonlinear function of the states \mathbf{x} and control inputs \mathbf{u} given by

$$\boldsymbol{\tau} = \boldsymbol{\Phi}(\mathbf{x}, \mathbf{u}), \quad (37)$$

where $\boldsymbol{\tau} \in \mathbb{R}^m$ is the control forces and moments vector and $\boldsymbol{\Phi} \in \mathbb{R}^{m \times p}$ a nonlinear mapping as a function of the states and control inputs. In this general form, Eq. (5) is changed to

$$\begin{aligned} \dot{\mathbf{x}} &= \mathbf{f}(\mathbf{x}) + \mathbf{g}(\mathbf{x}) \boldsymbol{\tau} = \mathbf{f}(\mathbf{x}) + \mathbf{g}(\mathbf{x}) \boldsymbol{\Phi}(\mathbf{x}, \mathbf{u}), \\ \mathbf{y} &= \mathbf{x}. \end{aligned} \quad (38)$$

Applying INDI using Eq. (13), the control law is then defined as

$$\Delta \mathbf{u} = \mathbf{g}^{-1}(\mathbf{x}) \left[\frac{\partial \boldsymbol{\Phi}(\mathbf{x}, \mathbf{u})}{\partial \mathbf{u}} \right]^{-1} (\mathbf{v}(\mathbf{x}) - \dot{\mathbf{y}}_0). \quad (39)$$

The DEP aircraft is over-actuated, meaning that the number of control inputs is larger than the number of controlled outputs ($p > m$). Therefore, $\boldsymbol{\Phi}$ in Eq. (39) is not square and thus not invertible, requiring the use of control allocation. The next sections will lay out the INCA algorithm used for this purpose and discuss the specific implementation for the DEP aircraft.

A. Incremental Nonlinear Control Allocation

INCA allocates incremental control inputs $\Delta \mathbf{u}$, while satisfying constraints on the control inputs. A secondary objective is introduced, so that the underdetermined allocation problem has a unique solution. To make the notation in Eq. (39) more compact, define the control effectiveness Jacobian (CEJ) as

$$\nabla_{\mathbf{u}} \Phi(\mathbf{x}_0, \mathbf{u}_0) = \frac{\partial \Phi(\mathbf{x}_0, \mathbf{u}_0)}{\partial \mathbf{u}}, \quad (40)$$

using the Jacobian ∇ . The CEJ is updated at every time step, thereby capturing nonlinearities and control effector interactions. The commanded incremental force and moment vector is defined as

$$\Delta \boldsymbol{\tau}_c = \mathbf{g}(\mathbf{x}_0)^{-1}(\mathbf{v}(\mathbf{x}) - \dot{\mathbf{y}}_0), \quad (41)$$

so that the incremental control allocation problem is defined as follows. Given the current state \mathbf{x}_0 , the current control input \mathbf{u}_0 and the incremental commanded force and moment vector $\Delta \boldsymbol{\tau}_c$, determine the incremental control input $\Delta \mathbf{u}$ so that

$$\begin{aligned} \nabla_{\mathbf{u}} \Phi(\mathbf{x}_0, \mathbf{u}_0) \Delta \mathbf{u} &= \Delta \boldsymbol{\tau}_c, \\ \text{subject to } \underline{\Delta \mathbf{u}} &\leq \Delta \mathbf{u} \leq \overline{\Delta \mathbf{u}}. \end{aligned} \quad (42)$$

Here $\underline{\Delta \mathbf{u}}$ and $\overline{\Delta \mathbf{u}}$ are the upper and lower incremental control input bounds, based on the position and rate constraints of the actuators, as defined in Table 1.

As stated in [21], the allocation problem defined in Eq. (42) can be solved with different methods of which QP gives the best allocation performance. Defining QP as a mixed optimization problem [25] gives

$$\begin{aligned} \min_{\Delta \mathbf{u}} & \underbrace{\|\mathbf{Q} (\nabla_{\mathbf{u}} \Phi(\mathbf{x}_0, \mathbf{u}_0) \Delta \mathbf{u} - \Delta \boldsymbol{\tau}_c)\|_2^2}_{\text{Allocation problem}} + \underbrace{\|\mathbf{W}(\Delta \mathbf{u} - \Delta \mathbf{u}_p)\|_2^2}_{\text{Secondary objective}}, \\ \text{subject to } & \underline{\Delta \mathbf{u}} \leq \Delta \mathbf{u} \leq \overline{\Delta \mathbf{u}}, \end{aligned} \quad (43)$$

where the weighting matrices \mathbf{Q} and \mathbf{W} are introduced, with $\mathbf{Q} \gg \mathbf{W}$, to prioritize the allocation problem over the secondary objective. The secondary objective is defined with the control preference vector \mathbf{u}_p , driving the control inputs to their trim values. Different algorithms can be used to solve Eq. (43), of which the active set method converges to the optimal solution in a finite number of steps. Furthermore, the method is computationally efficient for problems up to $\mathbf{u} \in \mathbb{R}^{15}$ [39]. Therefore, the active set algorithm is used to solve the allocation optimization problem.

B. Control allocation for translational and rotational control

Using the control force and moment vector $\boldsymbol{\tau}$, the incremental EoM for combined translational and rotational control are defined as

$$\begin{aligned} \dot{\mathbf{y}} &\approx \dot{\mathbf{y}}_0 + \mathbf{g}(\mathbf{x}_0) \Delta \boldsymbol{\tau}, \\ &\approx \dot{\mathbf{y}}_0 + \mathbf{g}(\mathbf{x}_0) \nabla_{\mathbf{u}} \Phi(\mathbf{x}_0, \mathbf{u}_0) \Delta \mathbf{u}, \end{aligned} \quad (44)$$

where

$$\mathbf{y} = \mathbf{x} = \begin{bmatrix} \bar{\mathbf{x}}_1 & \mathbf{x}_3 \end{bmatrix}^T = \begin{bmatrix} V & \gamma & p & q & r \end{bmatrix}^T, \quad (45)$$

and

$$\mathbf{g}(\mathbf{x}) = \begin{bmatrix} \text{diag}(0 & 0 & \mathbf{I}^{-1}) \end{bmatrix}, \quad (46)$$

and

$$\boldsymbol{\tau} = \begin{bmatrix} \dot{V} & \dot{\gamma} & l & m & n \end{bmatrix}^T, \quad (47)$$

and

$$\mathbf{u} = \begin{bmatrix} \alpha_{\text{des}} & \delta_{aL} & \delta_{aR} & \delta_e & \delta_r & n_{p1} & n_{p2} & n_{p3} & n_{p4} & n_{p5} & n_{p6} \end{bmatrix}^T. \quad (48)$$

Note that when comparing Eq. (1) and Eq. (48), α_{des} is now added to allow for controlling the altitude h . Note that α_{des} cannot be controlled directly but is as desired value, used as a reference in the aerodynamic attitude controller. The control loop for reference tracking of \mathbf{y}_{ref} , as defined in Eq. (19), is illustrated in Fig. 3. The altitude controller corresponds to controller 1 and the aerodynamic attitude controller to controller 3 in Fig. 2. Note how the translational and rotational control loop, defined in Sec. V, are merged in the INCA block and α_{des} is fed back as a reference value. Also, PCH is implemented by replacing $\mathbf{g}(\mathbf{x}_0)$ in Eq. (18) with $\nabla_{\mathbf{u}} \Phi(\mathbf{x}_0, \mathbf{u}_0) \Delta \mathbf{u}$ to ensure that the force and moment commands send to the INCA controller are achievable.

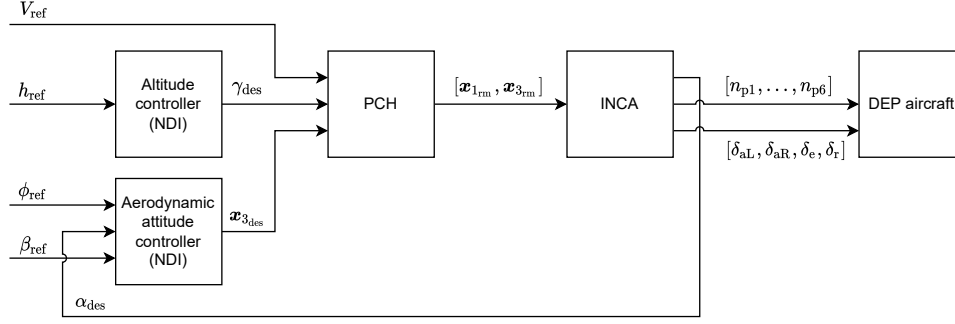


Fig. 3 Control loop structure with the outer loops and INCA controller for reference tracking.

The CEJ used in the INCA controller for translational and rotational control is defined as

$$\nabla_{\mathbf{u}} \Phi(\mathbf{x}_0, \mathbf{u}_0) = \begin{bmatrix} \left. \frac{\partial \dot{V}}{\partial u_1} \right|_{\mathbf{x}_0, \mathbf{u}_0} & \left. \frac{\partial \dot{V}}{\partial u_2} \right|_{\mathbf{x}_0, \mathbf{u}_0} & \cdots & \left. \frac{\partial \dot{V}}{\partial u_{11}} \right|_{\mathbf{x}_0, \mathbf{u}_0} \\ \left. \frac{\partial \dot{\gamma}}{\partial u_1} \right|_{\mathbf{x}_0, \mathbf{u}_0} & \left. \frac{\partial \dot{\gamma}}{\partial u_2} \right|_{\mathbf{x}_0, \mathbf{u}_0} & \cdots & \left. \frac{\partial \dot{\gamma}}{\partial u_{11}} \right|_{\mathbf{x}_0, \mathbf{u}_0} \\ \left. \frac{\partial l}{\partial u_1} \right|_{\mathbf{x}_0, \mathbf{u}_0} & \left. \frac{\partial l}{\partial u_2} \right|_{\mathbf{x}_0, \mathbf{u}_0} & \cdots & \left. \frac{\partial l}{\partial u_{11}} \right|_{\mathbf{x}_0, \mathbf{u}_0} \\ \left. \frac{\partial m}{\partial u_1} \right|_{\mathbf{x}_0, \mathbf{u}_0} & \left. \frac{\partial m}{\partial u_2} \right|_{\mathbf{x}_0, \mathbf{u}_0} & \cdots & \left. \frac{\partial m}{\partial u_{11}} \right|_{\mathbf{x}_0, \mathbf{u}_0} \\ \left. \frac{\partial n}{\partial u_1} \right|_{\mathbf{x}_0, \mathbf{u}_0} & \left. \frac{\partial n}{\partial u_2} \right|_{\mathbf{x}_0, \mathbf{u}_0} & \cdots & \left. \frac{\partial n}{\partial u_{11}} \right|_{\mathbf{x}_0, \mathbf{u}_0} \end{bmatrix}, \quad (49)$$

for the control input vector defined in Eq. (48). This matrix takes into account all effects of the control inputs on the controlled outputs, whereas for the general INDI controller only the primary effects are considered. Secondary effects, as the increase in drag because of control surface deflections, are then considered as disturbances [27]. A numerical example of the CEJ at the trim conditions is given in Eq. (60).

C. Control allocation for minimal propeller power

The traditional formulation of the INCA algorithm, using the control preference vector \mathbf{u}_p in Eq. (43), can be modified to optimize for different secondary objectives. Based on the method given in [40], synthesizing the translational and rotational control loop, the optimal control inputs for minimal propeller power can be calculated, while satisfying the reference trajectory defined in Eq. (19). For this, the INCA optimization problem is redefined as

$$\begin{aligned} \min_{\Delta \mathbf{u}} \quad & \|\mathbf{Q} (\nabla_{\mathbf{u}} \Phi(\mathbf{x}_0, \mathbf{u}_0) \Delta \mathbf{u} - \Delta \tau_c)\|_2^2 + \|\mathbf{W} (\nabla_{\mathbf{u}} \Omega(\mathbf{x}_0, \mathbf{u}_0) \Delta \mathbf{u} + \mathbf{P}_0)\|_2^2, \\ \text{subject to} \quad & \underline{\Delta \mathbf{u}} \leq \Delta \mathbf{u} \leq \overline{\Delta \mathbf{u}}, \end{aligned} \quad (50)$$

where

$$\nabla_{\mathbf{u}} \Omega(\mathbf{x}_0, \mathbf{u}_0) = \begin{bmatrix} 0 & \cdots & 0 & \text{diag} \left(\frac{\partial P_{p1}}{\partial n_{p1}}, \frac{\partial P_{p2}}{\partial n_{p2}}, \frac{\partial P_{p3}}{\partial n_{p3}}, \frac{\partial P_{p4}}{\partial n_{p4}}, \frac{\partial P_{p5}}{\partial n_{p5}}, \frac{\partial P_{p6}}{\partial n_{p6}} \right) \end{bmatrix}. \quad (51)$$

The $\nabla_{\mathbf{u}} \Omega(\mathbf{x}_0, \mathbf{u}_0)$ matrix is called the power effectiveness matrix, which describes the incremental change in propeller power P_p for an increase in propeller rotational velocity n_p . The vector \mathbf{P}_0 gives the current propeller power.

Solving the control allocation problem with Eq. (50) gives the optimal control distribution for minimal propeller power. Increasing the angle of attack α or the control deflections δ will increase the drag. This means that extra thrust is required to satisfy $\Delta \tau_c$, for $\Delta \dot{V}$ in particular, thereby increasing n_p and thus propeller power. Furthermore, using the propellers for roll or yaw control will also increase propeller power, as n_p for that specific propeller is increased. Using the above formulation thus gives the optimal trade-off between using the angle of attack α , the control surfaces δ and the propeller differential thrust and PAI effects by changing the propeller rotational velocities n_p , for minimal propeller power given a reference trajectory.

D. Model predictive control to compensate for actuator dynamics

An important limitation found during implementation of the INCA controller, is that the combination of rate constraints Eq. (2) with actuator dynamics Eq. (3) results in an over-conservative design. These rate constraints set a bound on $\Delta \mathbf{u}$ and $\Delta \dot{\mathbf{u}}$. If actuator dynamics are added, the achieved incremental control input $\Delta \mathbf{u}_a$ is smaller than the commanded incremental control input $\Delta \mathbf{u}_c$, which has two consequences. Firstly, the full potential of the DEP aircraft is not used as the achieved control inputs \mathbf{u}_a are lower, reducing the tracking performance. Secondly, the commanded incremental control input $\Delta \mathbf{u}_c$ is optimized for propeller power, but this is not achieved, so that the actual increase in efficiency is less. To solve this, an MPC controller is introduced to compensate for the actuator dynamics, using a similar method as in [26], redefining it for an incremental control input $\Delta \mathbf{u}$.

The method of MPC is based on optimal control methods as the linear-quadratic regulator (LQR). For these methods, the optimal control input \mathbf{u} is calculated using an optimization function. Compared to LQR, the main advantage of MPC is that state, input and output constraints can be incorporated. In the actuator dynamics framework, this means that actuator saturation can be prevented by limiting the control inputs with the constraints. Also, nonlinear actuator dynamics can be taken into account, as the MPC controller uses a finite horizon optimization. The objective function for optimal control is defined in quadratic form with two objectives, where the first ensures tracking and the second minimizes the use of the control inputs [41]. Weighing matrices \mathbf{Q} and \mathbf{R} are added to penalize the first or second objective. Constraints are added to this optimization, so that future state estimations satisfy the dynamic equations and stay within a feasible set. Also, constraints are added to the control inputs, so that they stay within their physical limits [42]. As new control inputs are calculated every time step with a receding horizon, feeding back actuator states, possible mismatches between the predicted and real output due to modeling errors and disturbances can be compensated for [43].

An important aspect to consider is that for MPC all current actuator states need to be known. Generally, these cannot all be measured and are subject to process and measurement noise. Therefore, a state-estimator is required, for which the Kalman filter is used. This is a recursive filter that gives an unbiased minimum variance estimate of a linear dynamic system taking into account both process and measurement noise [44]. The filter can be enhanced using the extended Kalman filter [45] and iterated extended Kalman filter [46] to take into account nonlinear system dynamics.

For implementation of MPC with incremental control inputs, the transfer function from $\Delta \mathbf{u}_a$ to \mathbf{u}_a needs to be defined, which is given by the dashed block in Fig. 4. The closed loop actuator dynamics transfer function $H(s)$, which is a single-input single output system for each actuator, is defined as

$$\frac{u_a(s)}{\Delta u_a(s)} = H(s) = \frac{A(s)}{1 - A(s)}, \quad (52)$$

where $A(s)$ is defined by Eq. (3). The system dynamics are discretized using zero-order hold so that they can be used in the MPC framework.

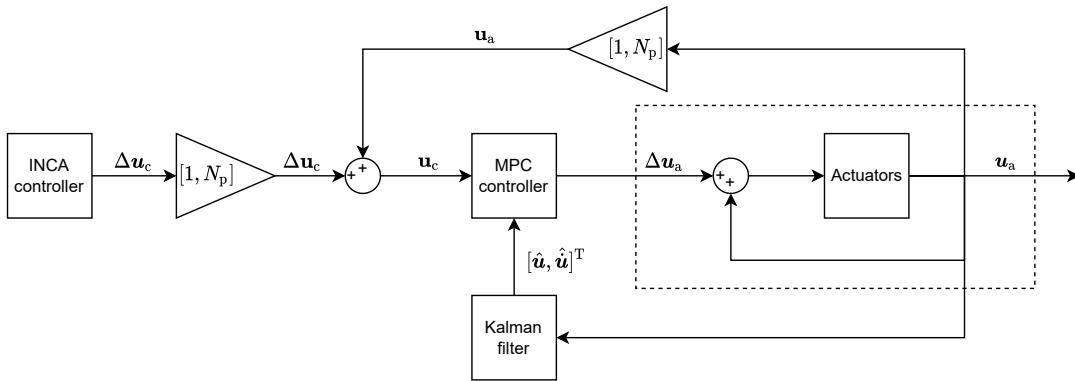


Fig. 4 Controller structure of MPC for actuator dynamics compensation. The closed loop transfer function of the actuator is given in the dashed line block.

The reference signal send to the MPC controller is $\mathbf{u}_c = \mathbf{u}_a + \Delta \mathbf{u}_c$, the sum of the current actual control input and the commanded incremental control input of the INCA controller. The MPC controller then minimizes the error between \mathbf{u}_a and \mathbf{u}_c , so that the commanded control inputs by the INCA controller are actually achieved. The control horizon is set to $N_c = 1$ as the reference should be reached as fast a possible. The prediction horizon is set to $N_p = 3$, giving

a fast response with feasible $\Delta \mathbf{u}_a$ and minimal computational effort. Note that the triangle blocks in Fig. 4 represent augmentation of the signal over the prediction horizon N_p , so that

$$\Delta \mathbf{u}_c = \begin{bmatrix} \Delta \mathbf{u}_c & 2\Delta \mathbf{u}_c & 3\Delta \mathbf{u}_c \end{bmatrix} \in \mathbb{R}^{p \times N_p}, \quad (53)$$

$$\mathbf{u}_a = \begin{bmatrix} \mathbf{u}_a & \mathbf{u}_a & \mathbf{u}_a \end{bmatrix} \in \mathbb{R}^{p \times N_p}, \quad (54)$$

adding the commanded incremental control input $\Delta \mathbf{u}_c$ over the prediction horizon N_p .

As the value of $\Delta \mathbf{u}_a$ should not be penalized, the weight on the control inputs was set to $\mathbf{R} = 0$. The weight on reference tracking of \mathbf{u}_c was set to $\mathbf{Q} = 1$, giving satisfactory tracking performance. As can be seen in the control loop of Fig. 4, a Kalman filter is placed giving the state estimates $\hat{\mathbf{u}}$ and $\hat{\hat{\mathbf{u}}}$, where the noise was assumed to be uncorrelated zero-mean white noise with variance one. Constraints are added on the output of the MPC controller so that

$$\underline{\mathbf{u}} \leq \mathbf{u}_a \leq \bar{\mathbf{u}}, \quad (55)$$

which ensures that the actuators do not saturate. These constraints were softened using a relaxation factor to guarantee that a feasible solution can always be found. Note that PCH is also used when implementing MPC, as the commanded control forces and moments can still be unachievable because of actuator limits.

VII. Simulations and Results

In this section, the INDI controller described in Sec. V is compared in simulation with the new INCA controller described in Sec. VI. The INDI controller does not use the differential thrust and PAI effects actively, so that all propellers produce the same thrust. This is an inherent limitation of any non-control allocation approach. The INCA controller does include these extra control effectors. It will be shown how the INCA controller uses this freedom to find control inputs that minimize propeller power for the same reference trajectory.

For the simulation, the flat-earth, six-degree-of-freedom equations of motion (EoM) are used to describe the attitude and position of the aircraft [36]. Simulations were initialized in MATLAB and run in Simulink at a sampling frequency of $f_s = 100$ Hz. Following the method of [33], it was found that at this sampling rate the influence of the perturbation term $\lambda(\mathbf{x}, \Delta t)$ in Eq. (14) can be discarded, so that stability of the INDI controller can be guaranteed.

A. Controller gains

A proportional gain matrix \mathbf{K} is used to steer the states to their reference values. The gains used for the INDI and INCA controller are given in Table 4 and the reference model gains defined for PCH in Table 5.

Table 4 Proportional gains

	h	V	γ	ϕ	α	β	p	q	r
INDI	0.2	0.2	0.5	0.8	2.0	1.0	30	5.0	30
INCA	0.3	1.0	1.0	1.0	2.0	1.0	30	5.0	30

Table 5 Reference model gains

	rm_V	rm_γ	rm_p	rm_q	rm_r
INDI	1.0	0.4	6.0	5.0	5.0
INCA	2.0	2.0	6.0	5.0	5.0

The gains are tuned to give the same rise time of approximately 2.4 s for a reference step of 35° on the roll angle ϕ , while minimizing the overshoot of the INDI controller. The roll angle of 35° is based on a rate 1-turn of the Airbus A320, scaled with the Froude number for $n = 1/8.5$ [3]. If the gains are further increased, which gives faster responses, the INDI controller saturates as it does not use the differential thrust and PAI effects and thus has less control authority.

This means that the required control forces and moments cannot be achieved, resulting in overshoot. The weighing matrices of Eq. (50) were set to

$$\mathbf{Q} = 10 \left[\text{diag} \left(m \quad 10 \cdot I_{yy} \quad 1 \quad 1 \quad 1 \right) \right], \quad (56)$$

$$\mathbf{W} = \mathbf{I}_6, \quad (57)$$

and when the reference altitude is changed, the weight on γ is decreased to $5 \cdot I_{yy}$.

B. Reference trajectory

The reference trajectory is specified with the vector in Eq. (19). Two reference trajectories were defined, where for the first the reference altitude is set equal to $h_{\text{ref}} = 300 \text{ m}$ and the velocity to $V_{\text{ref}} = 45 \text{ m/s}$, which are the cruise conditions. A square-wave reference signal with amplitude 35° is applied on ϕ_{ref} , while keeping the sideslip angle $\beta_{\text{ref}} = 0^\circ$ for most efficient flight. This allows showing how the DEP aircraft uses the control surfaces, differential thrust and PAI effects while maintaining constant altitude and velocity as efficiently as possible. For the second trajectory, the reference altitude is increased twofold from $h_{\text{ref}} = 300$ to 500 and 700 m . The reference velocity is also increased twofold from $V_{\text{ref}} = 40$ to 45 and 55 m/s . Simultaneously, a 35° full turn is specified, which combined results in a spiral trajectory. This second trajectory will show controller performance over a large part of the flight envelope, demonstrating how the nonlinear controller can deal with changing operating conditions.

C. Results

The tracking performance of the reference variables \mathbf{y}_{ref} for the first reference trajectory is given in Fig. 5 up to and including Fig. 8. As both controllers are tuned for the same rise time of ϕ without overshoot, no significant difference can be seen in Fig. 7 and Fig. 8. Interesting to note is that the tracking performance for the velocity and altitude is significantly improved for the INCA controller, as can be seen in Fig. 5 and Fig. 6. This is because the INCA controller merges the translational and rotational loop, controlling these reference values simultaneously. Also, in the INDI controller, the secondary effects of the control surfaces, affecting the velocity and altitude, are considered as disturbances. For the INCA controller, these are taken into account in the CEJ defined in Eq. (49), giving improved tracking performance.

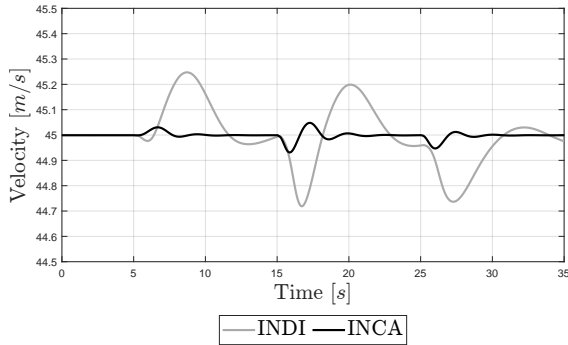


Fig. 5 Velocity V tracking performance.

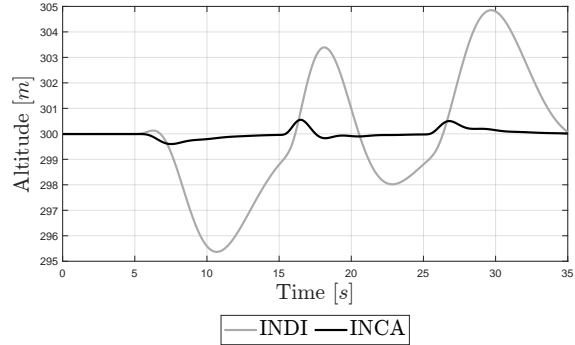


Fig. 6 Altitude h tracking performance.

These results can be confirmed with the root mean squared error (RMSE) values of the reference and desired states, given in Table 6, Table 7 and Table 8. Again, this shows that tracking performance is improved, especially for the altitude h , where the RMSE value is significantly lower for the INCA compared to the INDI controller.

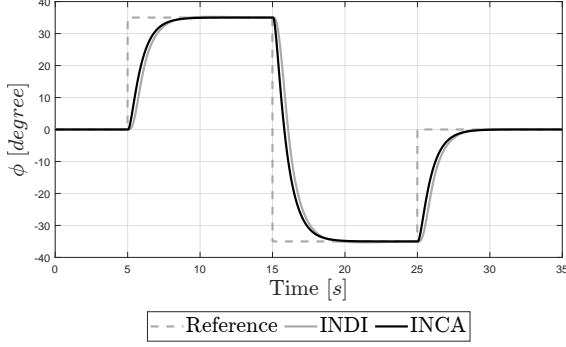


Fig. 7 Roll angle ϕ tracking performance.

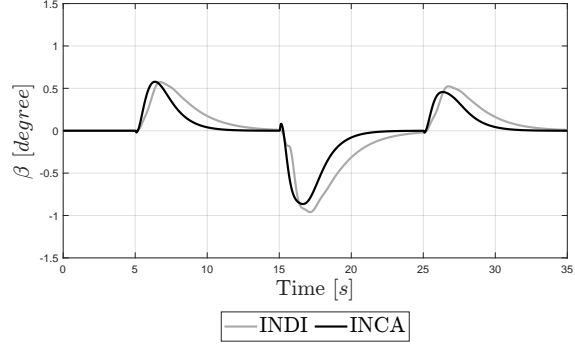


Fig. 8 Sideslip angle β tracking performance.

Table 6 Tracking performance x_1 .

RMSE($\epsilon_{\text{track}}(\mathbf{x}_1)$)		
Controller	INDI	INCA
V [m/s]	0.117	0.015
h [m]	2.421	0.180

Table 7 Tracking performance x_2 .

RMSE($\epsilon_{\text{track}}(\mathbf{x}_2)$)		
Controller	INDI	INCA
ϕ [°]	13.40	11.39
α [°]	0.705	0.359
β [°]	0.320	0.263
Total	7.747	6.582

Table 8 Tracking performance x_3 .

RMSE($\epsilon_{\text{track}}(\mathbf{x}_3)$)		
Controller	INDI	INCA
p [°/s]	0.142	0.152
q [°/s]	0.110	0.016
r [°/s]	0.006	0.019
Total	0.104	0.089

The control inputs for roll, yaw and velocity control are shown in Fig. 9 up to and including Fig. 11. Interesting to note is how the ailerons deflect less for the INCA controller, as compared to the INDI controller in Fig. 9. This is because part of the required rolling moment is now provided by the PAI effects. One can also observe the difference in rudder deflection in Fig. 10, where the yawing moment is now also provided by the differential thrust for the INCA controller. The total power of the propellers is given in Fig. 12, where one can see the power consumed is generally less for the INCA controller. This has two reasons, firstly the INCA controller uses the tip propellers more as can be seen in Fig. 11, which reduces the power consumed during cruise. Secondly, by using the differential thrust and PAI effects, the maneuvers can be performed more efficiently, therefore consuming less power. This can be seen between ten and fifteen seconds and between twenty and twenty-five seconds, where the INCA controller finds a constant allocation for minimal propeller power. In comparison, for the INDI controller the propeller power keeps oscillating at higher values. Interesting to see is that the propeller power of the INDI controller also sometimes drops below the levels of the INCA controller. At these moments, V_{ref} and h_{ref} are not accurately tracked, resulting in less propeller power but also deterioration in tracking performance. Compensating for this tracking error again results in a higher propeller power for the INDI controller.

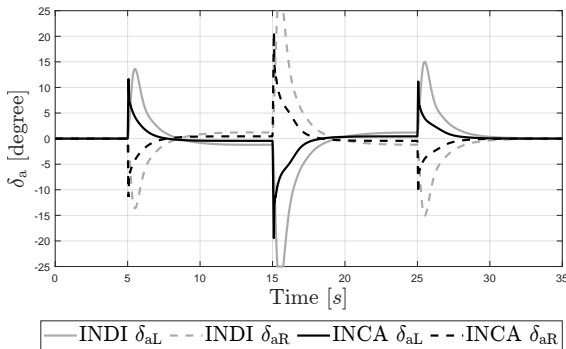


Fig. 9 Aileron deflection δ_a .

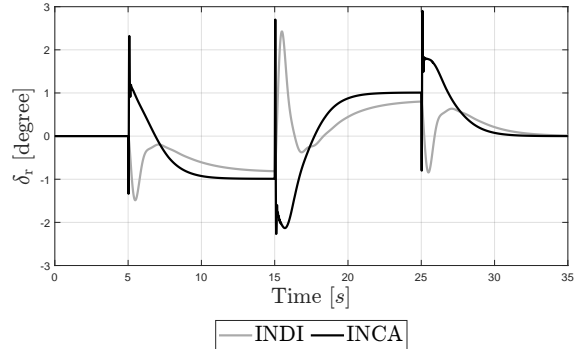


Fig. 10 Rudder deflection δ_r .

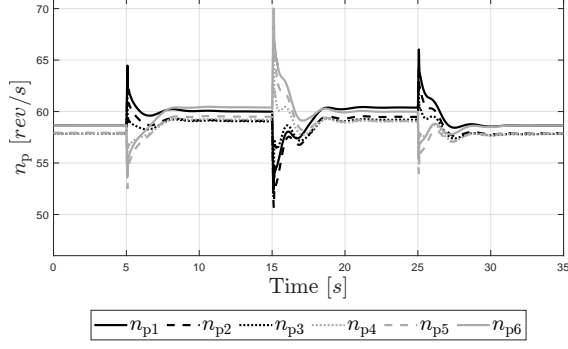


Fig. 11 Propeller rotational velocity n_p .

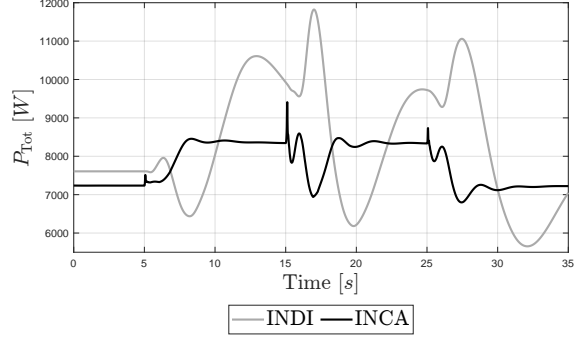


Fig. 12 Total propeller power P_{Tot} .

Integrating the total power gives the total energy consumed, which can be used to quantify the efficiency increase. The total energy consumed over the specified trajectory for the INDI controller is 0.290 MJ and for the INCA controller 0.273 MJ, giving an efficiency increase of approximately 6.1%. Note that this value is subject to a few assumptions, especially regarding the PAI effects. Also, this value can change based on a different set of controller gains and a different reference trajectory. Still, this shows that by actively using the extra control freedom of the DEP aircraft, optimizing for propeller power, a significant increase in efficiency can be achieved.

To illustrate the effect of the MPC controller, the incremental commanded and achieved left aileron deflections are given in Fig. 13 and Fig. 14, for the part of the response where the largest roll moment is required. Note that without MPC the rate constraints are removed, else the ailerons would move too slowly. As one can see in Fig. 13, the commanded $\Delta\delta_{aLc}$ is much larger than the achieved $\Delta\delta_{aLa}$. The same holds for the other control inputs, so that an offset is created between the commanded and achieved control allocation. Implementing MPC ensures that the achieved $\Delta\delta_{aLa}$ is much closer to the commanded $\Delta\delta_{aLc}$, as can be seen in Fig. 14. This illustrates how the MPC controller guarantees that the commanded control allocation from the INCA controller is achieved, which increases tracking performance and efficiency.

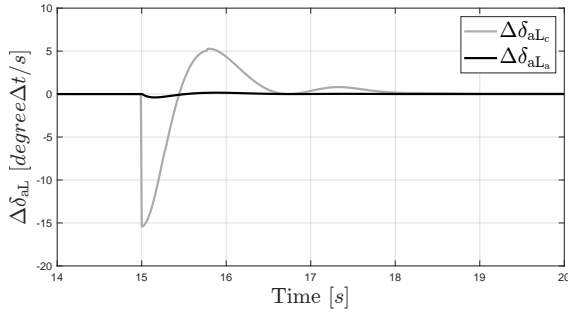


Fig. 13 Commanded and achieved incremental aileron deflection without MPC.

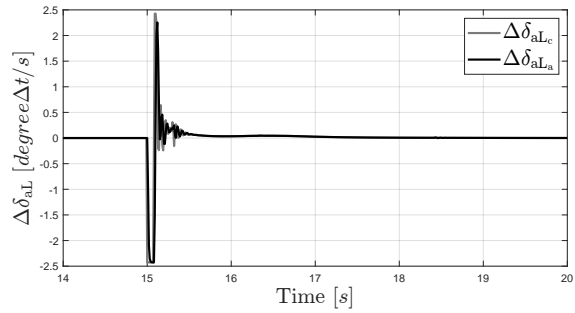


Fig. 14 Commanded and achieved incremental aileron deflection with MPC.

To show performance over a large part of the flight envelope, the second trajectory is used as the reference. The tracking performance for this trajectory is shown in Fig. 15 up to and including Fig. 17. Note that the maximum flight path angle is set to $\gamma_{max} = 10^\circ$, which explains the offset between reference and actual altitude in Fig. 17. Looking at Fig. 18, one can see that by using the differential thrust and PAI effects, more efficient flight is achieved. These results confirm that by using a nonlinear controller, performance at different operating points is guaranteed. The INCA controller in combination with MPC can thus be used to find the optimal control input distribution for multiple operating conditions within the flight envelope.

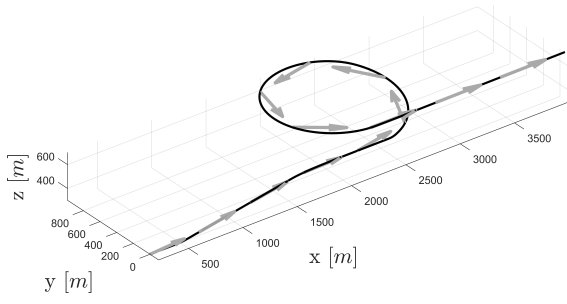


Fig. 15 Position in F_E frame.

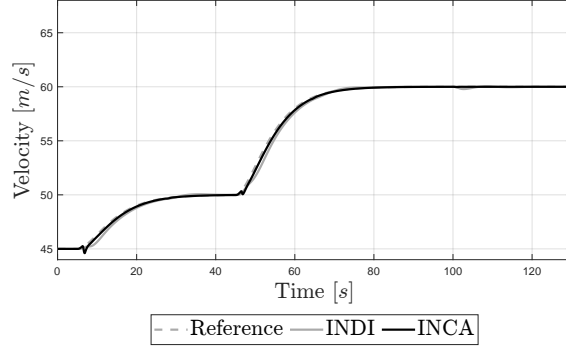


Fig. 16 Velocity m/s tracking performance.

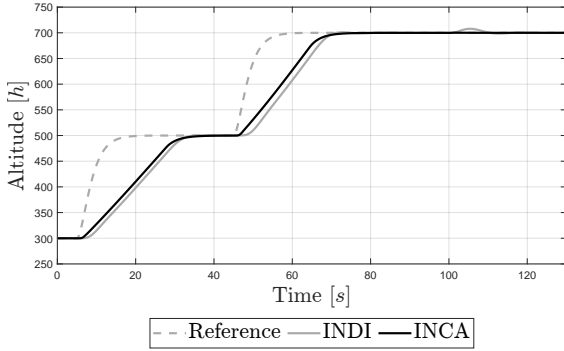


Fig. 17 Altitude h tracking performance.

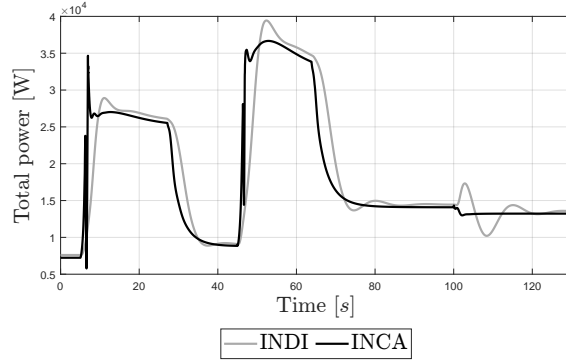


Fig. 18 Total propeller power P_{Tot} .

D. Robustness against delays and modeling errors

In the derivation of the MPC controller combined with INCA, it was assumed that the state derivatives can be measured instantaneously. This makes the method sensitive to delays introduced by filtering of the sensor measurements [47, 48]. A solution to this can be direct angular accelerometer feedback [49], but measuring \dot{V} and $\dot{\gamma}$ directly may prove to be difficult when implementing this method. As sensor filtering introduces delays, it was evaluated whether the MPC controller can manage a delay of Δt on the measurements of $\dot{\mathbf{y}}$. It was found that by introducing these delays, the controller performance degrades. This is because the commanded incremental control inputs are determined with delayed sensor measurements. The MPC controller then compensates for the actuator dynamics and with these compensated control inputs, the reference variables are followed. As these control inputs lag behind the actual response because of the delayed measurements, the MPC controller keeps compensating in each sampling instant to achieve tracking. This results in severe oscillations in the control inputs, which is unacceptable.

A solution for this problem is to scale down the commanded incremental control input with

$$\begin{aligned} \Delta \mathbf{u}_{c, \text{scale}} &= k_{\text{MPC}} \Delta \mathbf{u}_c, \\ 0 < k_{\text{MPC}} < 1. \end{aligned} \quad (58)$$

With this method, the MPC controller compensation is smaller, which reduces control input oscillations due to delayed state derivatives. The factor k_{MPC} was determined in simulation for different delay values by tuning the value of k_{MPC} until the oscillations in the control input disappear. For a delay of Δt $k_{\text{MPC}} = 0.6$, for $2\Delta t$ $k_{\text{MPC}} = 0.3$ and for $3\Delta t$ $k_{\text{MPC}} = 0.2$ was found. Note that by implementing k_{MPC} , the power optimization is deteriorated, as the $\Delta \mathbf{u}_c$ commanded by the INCA controller is scaled down. Also, tracking performance is affected, as the commanded forces and moments are not achieved. This method, therefore, gives a trade-off between INCA performance and robustness to delays.

Another important aspect to consider is the effect of combining MPC with the INCA controller on the stability of the controller. To analyze stability, modeling errors were introduced in the CEJ. These errors are defined by an offset based on the maximum CEJ during the nominal response and a scaling factor on the current CEJ so that

$$\nabla_{\mathbf{u}} \hat{\Phi}(\mathbf{x}_0, \mathbf{u}_0) = k_{\text{offset}} \nabla_{\mathbf{u}} \Phi_{\text{max}} + k_{\text{scale}} \nabla_{\mathbf{u}} \Phi(\mathbf{x}_0, \mathbf{u}_0). \quad (59)$$

Here k_{offset} is the offset factor, which ranges between -0.3 and 3.0, and k_{scale} is the scale factor, which ranges between 0.5 and 5.0. If either of these values becomes too small, the values in the CEJ switch sign, causing instability. The gains for roll are increased, so that $K_\phi = 3$ and $rm_p = 10$. This leads to faster roll responses so that instability is investigated closer to the operating limits of the DEP aircraft, which gives more distinct results. To quantify these results, the root mean square error (RMSE) is determined for the reference variables of Eq. (19). The nominal, minimum and maximum RMSE values for each of the reference values are given in Table 9.

Table 9 RMSE values for modeling uncertainty in CEJ.

	Nominal			Minimum			Maximum		
	RMSE	Offset	Scale	RMSE	Offset	Scale	RMSE	Offset	Scale
V	0.044	-0.3	0.8	0.026	3.0	5.0	0.185		
h	0.414	-0.2	0.6	0.226	3.0	5.0	1.156		
ϕ	16.92	3.0	4.0	16.34	2.9	4.9	18.17		
β	0.241	-0.3	0.8	0.219	2.9	4.8	0.753		

One can notice that the controller gives stable reference tracking for a large range of offset and scaling errors. The CEJ can be significantly overestimated, and only at high values the RMSE values increase substantially. Also, as long as the CEJ does not switch sign it can be underestimated. This confirms the findings in [38], showing that the INCA controller is robust to large modeling uncertainties. Adding an actuator compensator increases the stability margins of an INDI controller [33], but an analytical proof for INCA with MPC is beyond the scope of this paper. Stability is, therefore, concluded based on the simulation results given in Table 9.

VIII. Conclusion

Controllers without control allocation are unable to exploit the full potential of the distributed electric propulsion (DEP) aircraft. This is because traditional aircraft controllers only use the control surfaces without the differential thrust and propulsion airframe interaction (PAI) effects. In this paper, a new control allocation method is presented. It is based on the incremental nonlinear control allocation (INCA) approach, where a real time updated Jacobian model is used to determine the control effectiveness of the control inputs. This allows taking into account nonlinearities and coupling effects, while solving an efficient quadratic optimization problem. This method is based on incremental nonlinear dynamic inversion (INDI), where state derivatives measurements are used to reduce the model dependency and increase robustness against external disturbances. The secondary objective of the traditional INCA optimization function was redefined, so that the control allocation is optimized for minimal propeller power, while satisfying the reference tracking variables. In the allocation algorithm, the translational and rotational control loops are merged, allowing to determine the optimal control input in one step. A problem with the INCA formulation is that the commanded control inputs are not achieved because of the actuator dynamics. Therefore, this paper implements a model predictive control (MPC) controller to compensate for the actuator dynamics, improving tracking performance and optimization for minimal propeller power.

The performance of the new INCA controller combined with MPC was compared against a conventional INDI controller that does not actively use the differential thrust and PAI effects. The INDI controller uses an outer loop for translational control and an inner loop for rotational control. Two reference trajectories were defined, where for the first the reference velocity and altitude were kept at constant values. For the second trajectory, these values were changed, so that controller performance over a larger part of the flight envelope with varying operating conditions can be analyzed. In both simulations, it was shown that by actively using the differential thrust and PAI effects, propeller power is significantly decreased, while achieving improved tracking performance. Robustness against state derivative measurement delays was investigated. Here it was shown that by scaling down the commanded incremental control inputs, small delays in combination with MPC actuator compensation are allowed. Also, modeling uncertainties were introduced, showing that stability of the controller can be concluded over a large range of errors in the control effectiveness Jacobian (CEJ).

Future work will focus on the implementation of the MPC method for actuator dynamics compensation, as this method depends on real time state derivative measurements. The method of scaling down commanded incremental control inputs deteriorates the tracking performance and power optimization, as the commanded and actual control

inputs are different. It should be further investigated how this scaling factor can be taken into account in the optimization and whether other methods are available to increase robustness against delays. Furthermore, MPC is computationally expensive, which means that the performance regarding computational requirements should be analyzed. Next to that, when new data from wind tunnel testing or computational fluid dynamics analysis becomes available, the aerodynamic model should be updated. Specifically, the PAI effects including propeller-control surface interactions are uncertain and more accurate models will give better optimization performance. Finally, it can be interesting to implement the presented method on other flying frameworks. In particular, transition vehicles with vertical thrust form an interesting framework, as there is a clear trade-off between using the wing's lift and vertical thrust. The most efficient allocation will depend on the flight condition and the method proposed in this paper is specifically suited for this.

Appendix

$$\nabla_{\mathbf{u}} \mathbf{\Omega}(\mathbf{x}_0, \mathbf{u}_0)_{\text{trim}} = \begin{bmatrix} -5.209 & 1.587 & 0 & -769.4 & 0 \\ -1.074 \cdot 10^{-9} & 0 & 225.7 & 2.924 \cdot 10^{-7} & -36.64 \\ 1.081 \cdot 10^{-9} & 0 & -228.4 & -2.924 \cdot 10^{-7} & 9.395 \\ 8.431 \cdot 10^{-4} & 0.093 & 1.797 \cdot 10^{-6} & -1.410 \cdot 10^3 & 1.822 \cdot 10^{-7} \\ -8.492 \cdot 10^{-9} & 0 & 188.0 & 7.176 \cdot 10^{-6} & -1.209 \cdot 10^3 \\ 0.017 & 3.543 \cdot 10^{-4} & 4.174 & 0 & 4.918 \\ 0.015 & 5.290 \cdot 10^{-4} & 3.585 & 0 & 2.767 \\ 0.015 & 3.657 \cdot 10^{-4} & 1.428 & 0 & 1.615 \\ 0.015 & 3.657 \cdot 10^{-4} & -1.428 & 0 & -1.615 \\ 0.015 & 5.290 \cdot 10^{-4} & -3.585 & 0 & -2.767 \\ 0.017 & 3.543 \cdot 10^{-4} & -4.174 & 0 & -4.918 \end{bmatrix}^T \quad (60)$$

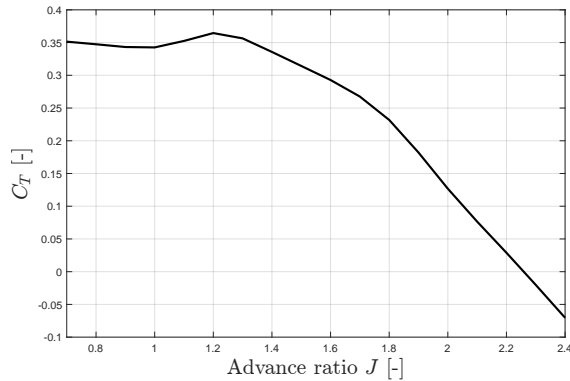


Fig. 19 Thrust coefficient C_T as a function of advance ratio J .

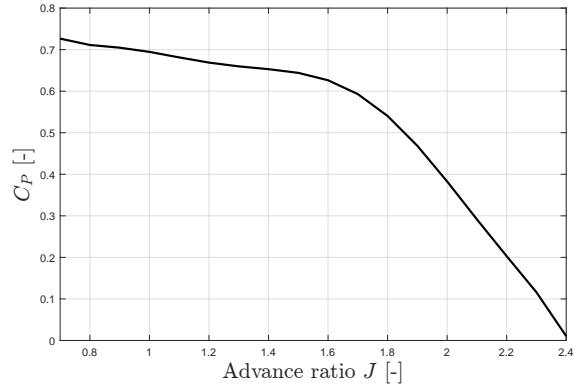


Fig. 20 Power coefficient C_P as a function of advance ratio J .

Acknowledgments

This work was partially funded by the European Union Horizon 2020 program, as part of the Clean Sky 2 program for Large Passenger Aircraft (CS2-LPA-GAM-2020/2021-01) under grant agreement No 945583.

References

- [1] DLR, "Strategic research and innovation agenda - The proposed European Partnership on Clean Aviation," Tech. rep., DLR, 2020.
- [2] EU, "Clean Sky 2 Development Plan Clean Sky 2 Joint Undertaking Development Plan," Tech. rep., EU, 2019.

- [3] Schmollgruber, P., Lepage, A., Bremmers, F., Jentink, H., Genito, N., Rispoli, A., Huhnd, M., and Meissner, D., “Towards validation of scaled flight testing,” *7th CEAS Air and Space Conference*, 2020, pp. 1–10.
- [4] Borer, N. K., Patterson, M. D., Viken, J. K., Moore, M. D., Clarke, S., Redifer, M. E., Christie, R. J., Stoll, A. M., Dubois, A., Bevirt, J. B., Gibson, A. R., Foster, T. J., and Osterkamp, P. G., “Design and performance of the NASA SCEPTOR distributed electric propulsion flight demonstrator,” *16th AIAA Aviation Technology, Integration, and Operations Conference*, 2016, pp. 3920–3939. <https://doi.org/10.2514/6.2016-3920>.
- [5] Pieper, K., Perry, A., Ansell, P., and Bretl, T., “Design and development of a dynamically, scaled distributed electric propulsion aircraft testbed,” *AIAA/IEEE Electric Aircraft Technologies Symposium*, 2018, pp. 1–22. <https://doi.org/10.2514/6.2018-4996>.
- [6] Kim, H. D., Perry, A. T., and Ansell, P. J., “A review of distributed electric propulsion concepts for air vehicle technology,” *AIAA/IEEE Electric Aircraft Technologies Symposium*, 2018, pp. 1–21. <https://doi.org/10.2514/6.2018-4998>.
- [7] Klunk, G. T., Freeman, J. L., and Schiltgen, B. T., “Vertical tail area reduction for aircraft with spanwise distributed electric propulsion,” *AIAA/IEEE Electric Aircraft Technologies Symposium*, 2018, pp. 5022–5034. <https://doi.org/10.2514/6.2018-5022>.
- [8] Freeman, J. L., and Klunk, G. T., “Dynamic flight simulation of spanwise distributed electric propulsion for directional control authority,” *AIAA/IEEE Electric Aircraft Technologies Symposium*, 2018, pp. 1–15. <https://doi.org/10.2514/6.2018-4997>.
- [9] Soikkeli, J. S. E., “Vertical tail reduction through differential thrust - An initial assessment of aeropropulsive effects on lateral-directional stability and control in engine inoperative conditions,” *Master's Thesis, Delft University of Technology, Delft, the Netherlands*, 2020.
- [10] Perry, A. T., Ansell, P. J., and Kerho, M. F., “Aero-propulsive and propulsor cross-coupling effects on a distributed propulsion system,” *Journal of Aircraft*, Vol. 55, No. 6, 2018, pp. 2414–2426. <https://doi.org/10.2514/1.C034861>.
- [11] Rothhaar, P. M., Murphy, P. C., Bacon, B. J., Gregory, I. M., Grauer, J. A., Busan, R. C., and Croom, M. A., “NASA langley distributed propulsion VTOL tilt-wing aircraft testing, modeling, simulation, control, and flight test development,” *14th AIAA Aviation Technology, Integration, and Operations Conference*, 2014, pp. 2999–3012. <https://doi.org/10.2514/6.2014-2999>.
- [12] Slotine, J., *Applied Nonlinear Dynamics*, 1st ed., Prentice-Hall Inc., 1991.
- [13] Enns, D., Stein, G., Bugajski, D., and Hendrick, R., “Dynamic inversion: an evolving methodology for flight control design,” *International Journal of Control*, Vol. 59, No. 1, 1994, pp. 71–91. <https://doi.org/10.1080/00207179408923070>.
- [14] Sieberling, S., Chu, Q. P., and Mulder, J. A., “Robust flight control using incremental nonlinear dynamic inversion and angular acceleration prediction,” *Journal of Guidance, Control, and Dynamics*, Vol. 33, No. 6, 2010, pp. 1732–1742. <https://doi.org/10.2514/1.49978>.
- [15] Jatiningrum, D., de Visser, C. C., van Paassen, M. M., and Mulder, M., “Modeling an angular accelerometer using frequency-response measurements,” *AIAA Guidance, Navigation, and Control Conference*, 2016, pp. 1–14. <https://doi.org/10.2514/6.2016-1139>.
- [16] Jatiningrum, D., van Paassen, M. M., de Visser, C. C., Chu, Q. P., and Mulder, M., “Investigating cross-axis sensitivity and misalignment in an angular accelerometer measurement unit,” *AIAA Guidance, Navigation, and Control Conference*, 2017, pp. 1–16. <https://doi.org/10.2514/6.2017-1905>.
- [17] Johansen, T. A., and Fossen, T. I., “Control allocation - A survey,” *Automatica*, Vol. 49, No. 5, 2013, pp. 1087–1103. <https://doi.org/10.1016/j.automatica.2013.01.035>.
- [18] Doman, D. B., and Sparks, A. G., “Concepts for constrained control allocation of mixed quadratic and linear effectors,” *American Control Conference*, 2002, pp. 3729–3734.
- [19] Bolender, M. A., and Doman, D. B., “Nonlinear control allocation using piecewise linear functions,” *Journal of Guidance, Control, and Dynamics*, Vol. 27, No. 6, 2004, pp. 1017–1027. <https://doi.org/10.2514/1.9546>.
- [20] Poonamallee, V. L., Yurkovich, S., Serrani, A., Doman, D. B., and Oppenheimer, M. W., “A nonlinear programming approach for control allocation,” *Proceedings of the American Control Conference*, 2004, pp. 1689–1694. <https://doi.org/10.23919/acc.2004.1386822>.
- [21] Matamoros, I., and de Visser, C. C., “Incremental nonlinear control allocation for a tailless aircraft with innovative control effectors,” *AIAA Guidance, Navigation, and Control Conference*, 2018, pp. 1116–1140. <https://doi.org/10.2514/6.2018-1116>.

- [22] Virnig, J. C., and Bodden, D. S., “Multivariable control allocation and control law conditioning when control effectors limit,” *Guidance, Navigation, and Control Conference*, 1994, pp. 572–582. <https://doi.org/10.2514/6.1994-3609>.
- [23] Buffington, J. M., and Enns, D. F., “Lyapunov stability analysis of daisy chain control allocation,” *Journal of Guidance, Control, and Dynamics*, Vol. 19, No. 6, 1996, pp. 1226–1230. <https://doi.org/10.2514/3.21776>.
- [24] Durham, W. C., “Constrained control allocation,” *Journal of Guidance, Control, and Dynamics*, Vol. 16, No. 4, 1993, pp. 717–725. <https://doi.org/10.2514/3.21072>.
- [25] Bodson, M., “Evaluation of optimization methods for control allocation,” *Journal of Guidance, Control, and Dynamics*, Vol. 25, No. 4, 2002, pp. 703–711. <https://doi.org/10.2514/2.4937>.
- [26] Luo Andrea, Y. S., and Yurkovich, S., “Model predictive dynamic control allocation with actuator dynamics,” *Proceeding of the 2004 American Control Conference*, 2004, pp. 1695–1700.
- [27] Lu, P., van Kampen, E. J., de Visser, C., and Chu, Q., “Aircraft fault-tolerant trajectory control using incremental nonlinear dynamic inversion,” *Control Engineering Practice*, Vol. 57, 2016, pp. 126–141. <https://doi.org/10.1016/j.conengprac.2016.09.010>.
- [28] Ruijgrok, G. J. J., *Elements of airplane performance*, 2nd ed., Delft University Press, 2009.
- [29] Veldhuis, L., “Propeller wing aerodynamic interference,” Ph.D. thesis, Delft University of Technology, 2005.
- [30] De Vries, R., Brown, M., and Vos, R., “Preliminary sizing method for hybrid-electric distributed-propulsion aircraft,” *Journal of Aircraft*, Vol. 56, No. 6, 2019, pp. 2172–2188. <https://doi.org/10.2514/1.C035388>.
- [31] Patterson, M. D., “Conceptual design of high-lift propeller systems for small electric aircraft,” Ph.D. thesis, Georgia Institute of Technology, 2016.
- [32] Sinnige, T., Van Arnhem, N., Stokkermans, T. C., Eitelberg, G., and Veldhuis, L. L., “Wingtip-mounted propellers: aerodynamic analysis of interaction effects and comparison with conventional layout,” *Journal of Aircraft*, Vol. 56, No. 1, 2019, pp. 295–312. <https://doi.org/10.2514/1.C034978>.
- [33] Wang, X., van Kampen, E.-J., Chu, Q., and Lu, P., “Stability analysis for incremental nonlinear dynamic inversion control,” *Journal of Guidance, Control, and Dynamics*, Vol. 42, No. 5, 2019, pp. 1116–1129. <https://doi.org/10.2514/1.g003791>.
- [34] Johnson, E. N., and Calise, A. J., “Pseudo-control hedging : a new method for adaptive control,” *Advances in Navigation Guidance and Control Technology Workshop*, 2000, pp. 1–23.
- [35] Simplicio, P., Pavel, M. D., van Kampen, E., and Chu, Q. P., “An acceleration measurements-based approach for helicopter nonlinear flight control using incremental nonlinear dynamic inversion,” *Control Engineering Practice*, Vol. 21, No. 8, 2013, pp. 1065–1077. <https://doi.org/10.1016/j.conengprac.2013.03.009>.
- [36] Stevens, B. L., Lewis, F. L., and Johnson, E. N., *Aircraft control and simulation*, 3rd ed., Wiley, New Jersey, 2016.
- [37] Durham, W., *Aircraft Flight Dynamics and Control*, 2nd ed., John Wiley & Sons Ltd., 2013.
- [38] Matamoros, I., “Nonlinear control allocation for a high-performance tailless aircraft with innovative control effectors - An incremental robust approach,” *Master’s Thesis, Delft University of Technology, Delft, the Netherlands*, 2017.
- [39] Petersen, J. A., and Bodson, M., “Constrained quadratic programming techniques for control allocation,” *IEEE Transactions on Control Systems Technology*, Vol. 14, No. 1, 2006, pp. 91–98. <https://doi.org/10.1109/TCST.2005.860516>.
- [40] Pfeifle, O., and Fichter, W., “Energy Optimal Control Allocation for INDI Controlled Transition Aircraft,” *AIAA SciTech Forum*, 2021, pp. 1457–1468. <https://doi.org/10.2514/6.2021-1457>.
- [41] Camacho, E. F., and Bordons, C. C., *Model predictive control*, 2nd ed., Springer, 2007.
- [42] Müller, M. A., and Allgöwer, F., “Economic and distributed model predictive control: recent developments in optimization-based control,” *SICE Journal of Control, Measurement, and System Integration*, Vol. 10, No. 2, 2017, pp. 39–52. <https://doi.org/10.9746/jcmsi.10.39>.
- [43] Findeisen, R., and Allgöwer, F., “An introduction to nonlinear Model predictive control,” *21st Benelux Meeting on Systems and Control*, 2002, pp. 119–141.

- [44] Verhaegen, M. M., and Verdult, V., *Filtering and system identification : a least squares approach*, 1st ed., Cambridge University Press, 2007.
- [45] Skoglund, M. A., Hendeby, G., and Axehill, D., “Extended Kalman filter modifications based on an optimization view point,” *18th Conference on Information Fusion*, 2015, pp. 1856–1861.
- [46] Barfoot, T. D., *State estimation for robotics*, 1st ed., Cambridge University Press, 2017.
- [47] Smeur, E. J., Chu, Q., and De Croon, G. C., “Adaptive incremental nonlinear dynamic inversion for attitude control of micro air vehicles,” *Journal of Guidance, Control, and Dynamics*, Vol. 39, No. 3, 2016, pp. 450–461. <https://doi.org/10.2514/1.G001490>.
- [48] Grondman, F., Looye, G. H., Kuchar, R. O., Chu, Q. P., and van Kampen, E. J., “Design and flight testing of incremental nonlinear dynamic inversion based control laws for a passenger aircraft,” *AIAA Guidance, Navigation, and Control Conference*, 2018, pp. 385–409. <https://doi.org/10.2514/6.2018-0385>.
- [49] Cakiroglu, C., Van Kampen, E. J., and Chu, Q., “Robust incremental nonlinear dynamic inversion control using angular accelerometer feedback,” *AIAA Guidance, Navigation, and Control Conference*, 2018, pp. 1128–1143. <https://doi.org/10.2514/6.2018-1128>.